Check for updates

JGR Atmospheres

RESEARCH ARTICLE
10.1029/2025JD044204

Special Collection:
Climate and weather extremes in a warming climate: Processes, Prediction and Projection

Development of a Virga Detection Tool and Associated Study of Arctic Virga and Precipitation

Lekhraj Saini[1], **Saurabh Das**[1], **and Nuncio Murukesh**[2]

[1]Department of Astronomy, Astrophysics and Space Engineering, Indian Institute of Technology Indore, Indore, Madhya Pradesh, India, [2]National Center for Polar and Ocean Research, Ministry of Earth Sciences, Vasco Da Gama, Goa, India

Abstract Virga is a meteorological phenomenon in which precipitation does not reach the ground due to evaporation or sublimation well above the surface. This significantly influences Earth's energy budget, weather forecasting, climate prediction, hydrology, civilization, and vegetation. Despite its importance, studies of virga and it's quantification are rare and limited due to the lack of observations. This study proposes a novel virga detection tool using the reflectivity (Ze) and Doppler velocity (W) profiles of the vertically pointing Micro Rain Radar (MRR). The method incorporates height and season dependent thresholds and validates outcomes with ground-based disdrometer observations, ensuring reliability and robustness. The detection tool was tested in Ny-Ålesund, a rapidly warming place in the Arctic region where virga studies are limited. The results indicate that the occurrence of virga varies between 25% and 40% between seasons, with evaporation occurring at lower heights in the cold season compared to summer. Virga is often observed before precipitation and leads to a dryer surface condition. The use of the proposed tool is expected to improve the accurate estimation of precipitation and better understanding of the virga process.

Plain Language Summary Virga occurs when precipitation falls from clouds but evaporates before reaching the ground. This phenomenon can affect the hydrological cycle, agriculture, and Earth's radiation and energy budgets. In some regions, frequent virga contributes to drought conditions, as seen in parts of Canada from 1999 to 2005. Accurately detecting virga is important, but satellite-based radars often struggle to observe precipitation near the surface, leading to errors. Ground-based instruments such as Micro Rain Radars (MRR) are essential for better detection. This study presents a new method using MRR data from Ny-Ålesund, Svalbard, to identify virga and surface precipitation. The method applies altitude and season specific thresholds to separate virga and surface precipitation. The results show that the 25%–40% precipitation completely evaporate before reaching the ground. It is observed that in Arctic, during the cold seasons, evaporation occurs closer to the surface, whereas in summer it is more frequent at higher levels. Surface precipitation is linked to low cloud bases (0.5–1 km), while virga is related to high cloud bases (>1 km). The combined use of the present algorithm and long-term ground-based observations from the Arctic will improve the understanding of Arctic precipitation processes.

Key Points:

- Developed a virga detection algorithm using MRR Reflectivity (Ze) and Doppler velocity (W) profiles
- In Ny-Ålesund, virga accounts for ~ 25%–40% of seasonal occurrence of virga and surface precipitation
- Peak occurrence of virga is observed at ~1–2 km in the cold seasons and ~3–4 km in the summer

Correspondence to:
S. Das,
das.saurabh01@gmail.com;
saurabh.das@iiti.ac.in

Citation:
Saini, L., Das, S., & Murukesh, N. (2026). Development of a Virga Detection tool and associated study of Arctic Virga and precipitation. *Journal of Geophysical Research: Atmospheres*, *131*, e2025JD044204. https://doi.org/10.1029/2025JD044204

Received 2 MAY 2025
Accepted 26 FEB 2026

Author Contributions:
Conceptualization: Lekhraj Saini, Saurabh Das
Data curation: Lekhraj Saini, Nuncio Murukesh
Formal analysis: Lekhraj Saini
Funding acquisition: Saurabh Das
Investigation: Lekhraj Saini
Methodology: Lekhraj Saini, Saurabh Das
Project administration: Saurabh Das, Nuncio Murukesh
Resources: Saurabh Das, Nuncio Murukesh
Software: Lekhraj Saini
Supervision: Saurabh Das, Nuncio Murukesh
Validation: Saurabh Das
Visualization: Lekhraj Saini
Writing – original draft: Lekhraj Saini
Writing – review & editing: Lekhraj Saini, Saurabh Das, Nuncio Murukesh

© 2026. American Geophysical Union. All Rights Reserved.

1. Introduction

Precipitation is a crucial component of Earth's radiative forcing and energy budget. Nevertheless, it has a significant impact on weather hazards, hydrology, and agriculture. However, not all precipitation reaches the ground. It is known as virga, which consists of rain, ice, or snow falling within the troposphere and completely evaporates or sublimates primarily due to dry air well above the surface (Beynon & Hocke, 2022). The prolonged drought in the Canadian Prairies during 1999–2005 highlights the critical role of virga, where precipitation frequently formed aloft but largely sublimated or evaporated within the dry sub-cloud layer, resulting in minimal or no surface precipitation (Evans et al., 2011; Roberts et al., 2006; Stewart et al., 2011). The evaporation of precipitation influences local energy budgets, as virga can cause notable changes in surface moisture and temperature profiles (Kalesse-Los et al., 2023). Radar and ceilometer measurements indicate that virga is often preceded by precipitation within the cloud layer (Jullien et al., 2020; Kalesse-Los et al., 2023). It is mainly produced by specific types of cloud, such as stratocumulus and convective cells, with varying depths of the cloud that affect the extent of evaporation (Yang et al., 2018). Although the detection and estimation of virga are essential for accurate weather predictions, it remains a challenge due to the limited observational study.

Previous studies have attempted to quantify the occurrence of virga precipitation globally using three space-borne radar observations, namely the Tropical Rainfall Measuring Mission (TRMM), Global Precipitation

21698996, 2026, 6, Downloaded from https://agupubs.onlinelibrary.wiley.com/doi/10.1029/2025JD044204 by Indian Institute of Technology Indore, Wiley Online Library on [08/04/2026]. See the Terms and Conditions (https://onlinelibrary.wiley.com/terms-and-conditions) on Wiley Online Library for rules of use; OA articles are governed by the applicable Creative Commons License

Measurement (GPM), and CloudSat (Saikranthi et al., 2014; Wang et al., 2018). The findings indicate that virga precipitation constitutes more than 30% according to TRMM and GPM, while CloudSat estimates it at 50%, particularly in arid regions where dry air leads to evaporation (Wang et al., 2018). In the polar region, the reanalysis and regional models estimate that approximately 17% of precipitation evaporates or sublimates on a continental scale, increasing to around 35% in coastal regions of Antarctica (Agosta et al., 2019; Grazioli et al., 2017). Virga accounts for nearly 50% (30%) of false precipitation detections by TRMM (GPM) satellites (Wang et al., 2018), mainly due to the blind zone of space borne radar near the surface, around 1.5 km, which introduces biases in total precipitation estimates (Maahn et al., 2014; Valdivia et al., 2022). Shates et al. (2025) used Ka-band Zenith Radar at the Atmospheric Radiation Measurement user facility on the North Slope of Alaska in the Arctic and revealed frequent virga misclassified as surface precipitation due to the CloudSat blind zone. In this context, ground-based vertical profilers play a crucial role with their high vertical resolution and continuous observations. Several studies have successfully used ground-based vertical profilers to detect virga, particularly in cold environments such as polar and high-latitude regions (Beynon & Hocke, 2022; Jullien et al., 2020). Kodamana and Fletcher (2021) used CloudSat–CPR retrievals to validate precipitation with ground observations and discovered around 9% virga in Canada.

Kalesse-Los et al. (2023) developed Virga-Sniffer, an open-source Python tool designed to detect virga from continuous ground-based remote-sensing observations, achieving 86% accuracy compared to CloudNet. CloudNet (CloudnetPy) provides standardized target classifications of cloud and precipitation hydrometeors from ground-based radar–lidar (Illingworth et al., 2007). The Virga-sniffer tool combines ceilometer data for cloud base height (CBH) detection with vertically pointing Doppler cloud radar to identify clouds and precipitation that partially or fully evaporate. Additional inputs, such as the lifting condensation level, a surface rain flag, and Doppler velocity fields, can be incorporated to refine the detection. The Virga-Sniffer has adjustable threshold settings and works well in multilayer cloud environments; however, the threshold remains fixed throughout the altitude once fixed. Since precipitation characteristics vary with both season and altitude, a season and height dependent thresholding approach may improve precipitation detection accuracy. Moreover, stand-alone radar-based algorithms will be particularly useful at sites where complementary measurements, such as ceilometer observations, are unavailable.

Virga studies in the Arctic remain underexplored due to the lack of observations and the unique challenges of conducting measurements in this region. Detecting virga, particularly snow virga, remains a significant challenge due to the low radar reflectivity of the ice particles and the intrinsic bias of conventional radar systems toward liquid precipitation (Saini et al., 2024, 2025b, 2025c). This study develops a new tool based on Micro Rain Radar (MRR) reflectivity (Ze) and Doppler velocity (W) profiles for virga identification. To test the technique, this study utilized data from Ny-Ålesund, one of the fastest-warming sites in the Arctic (Maturilli et al., 2013). The proposed technique uses a variable threshold with height and season for the detection of precipitation signals. The performance of the technique is validated against the ground-based disdrometer. This study aims to provide a crucial contribution to understanding precipitation processes in the Arctic. Initially, seasonal meteorological conditions are analyzed to characterize the vertical atmospheric structure over Ny-Ålesund. The virga detection algorithm is introduced and described with a representative summer virga case study. The seasonal occurrences of virga and surface precipitation are examined, including radar reflectivity profiles, evaporation height, and temporal differences between virga and precipitation. In addition, associated ground meteorological conditions and CBH are discussed to provide a better understanding of the characteristics of both virga and precipitation.

2. Data and Instruments

This study uses observational data for 2020–2024 for various atmospheric parameters collected at the Ny-Ålesund Research Station (78.9°N, 11.9°E, 40 m AMSL), a coastal site in the Arctic. The site is located on the southern shore of Kongsfjorden, one of the many deep and wide fjords on the west coast of Spitsbergen in the Svalbard (Saini et al., 2025b). Due to its position, its atmosphere is mainly influenced by the nearby orographic features and the diabatic heating of the warm ocean (Maturilli & Kayser, 2017).

Precipitation data from the Micro Rain Radar (MRR) and disdrometer, along with CBH measurements from a ceilometer, have been collected from the Gruvebadet Atmospheric Observatory near the Himadri Research Station in Ny-Ålesund, Svalbard. The ground-level meteorological conditions from the Automatic Weather Station (AWS) (2020–2024) and the vertical soundings from the Radiosonde (2017–2022) have been obtained

from the AWIPEV Research Station (0.8 km away) in Ny-Ålesund (Maturilli, 2020; Maturilli & Dünschede, 2023). The radiosonde observations are available at a temporal resolution of one sounding per day, launched around local noon (12:00 pm).

The following are the short details of each instrument, including operating principles, specifications, sensitivities, and limitations.

2.1. Micro Rain Radar

The MRR2 by METEK GmbH is a vertically pointed frequency modulated continuous wave radar operating on Doppler principle at 24.1 GHz. The MRR provides precipitation profiles up to 6 km altitude with a vertical resolution of 200 m across 32 range gates (Kneifel et al., 2011; Peters et al., 2002). The MRR has a nominal sensitivity of around +3 dBZ, although constraints in Doppler moment quality, spurious errors, and receiver noise frequently impact raw spectra. To resolve this, a sophisticated post-processing approach that is especially optimized for snow observations was used, named ImProToo (Maahn & Kollias, 2012). By determining the most prominent spectral peak, this technique eliminates noise and uses a dynamic dealiasing procedure to enable measurements even when the Nyquist velocity range is exceeded. This improved processing increases the effective sensitivity to approximately −14 dBZ in short ranges and −8 dBZ in longer ranges. This enhancement exploits the full hardware potential of MRR2 and enables the retrieval of Ze and W, extending its applicability to shallow, solid precipitation, and virga processes (Maahn & Kollias, 2012).

2.2. OTT Parsivel^2 Disdrometer

Surface precipitation was observed using the **Par**ticle **Si**ze and **Vel**ocity (Parsivel^2) optical disdrometer by OTT GmbH. It records a 32 × 32 matrix of droplet sizes (0.06–24.5 mm) and Doppler velocities (0.05–20.8 ms^{-1}) (Löffler-Mang & Joss, 2000; Ott parsivel-2 disdrometer manual, 2023). Observations of hydrometeors crossing the 1 mm horizontal laser beam of 720 nm within a sensor area of 180 × 30 mm^2.

Some limitations of Parsivel^2 include uncertainty for non-spherical particles such as snow and graupel, potential contamination from blowing snow during blizzards, and wind-induced tilt trajectories that might bias retrievals (Battaglia et al., 2010; Sarkar et al., 2015; Tokay et al., 2014). In accordance with other research employing Parsivel^2 or Thies disdrometers for snowfall analysis, a lower threshold of 0.1 mmh^{-1} precipitation rate (Cha & Yum, 2020; Garcia-Benadi et al., 2020; Maahn & Kollias, 2012) with a temporal resolution of 6 min was used to reduce such effects.

2.3. Ceilometer

CBH was observed using a vertically profiling light detection and ranging ceilometer (CL51 by Vaisala) that works on 910 nm wavelength. Vertically moving laser pulses scatter back from Haze, fog, mist, virga, precipitation, and clouds particles. This backscattered light is measured by the device and generates a vertical signal intensity (backscatter coefficient) profile. The ceilometer calculates the CBH by measuring the maximum backscatter signature (Source: https://docs.vaisala.com/r/M210801EN-K/en-US) up to three layers, CBH1, CBH2, and CBH3. The lowest cloud base is CBH1, which is followed by CBH2 and CBH3. Although the ceilometer can detect CBH1 with good accuracy, it is typically unable to identify higher cloud bases due to its limited range and signal attenuation in thick clouds or during precipitation. The ceilometer has a maximum range 7.7 km with vertical resolution of 10 m and temporal resolution of 6 s (Maturilli & Ebell, 2018; Oyj, 2022).

3. Methodology

Figure 1 presents a flowchart outlining the algorithm, which is structured into two distinct phases: data pre-processing and Virga detection. The data pre-processing phase involves processing, averaging, and generating thresholds from MRR vertical profiles to establish reference parameters. In the Virga Detection phase, specific criteria are used to identify virga occurrences based on the thresholds derived in the initial step and refine the detected results by evaluating each threshold against disdrometer observations, selecting the most appropriate threshold to generate the final output. A detailed explanation of different stages is given below.

21698996, 2026, 6, Downloaded from https://agupubs.onlinelibrary.wiley.com/doi/10.1029/2025JD044204 by Indian Institute of Technology Indore, Wiley Online Library on [08/04/2026]. See the Terms and Conditions (https://onlinelibrary.wiley.com/terms-and-conditions) on Wiley Online Library for rules of use; OA articles are governed by the applicable Creative Commons License

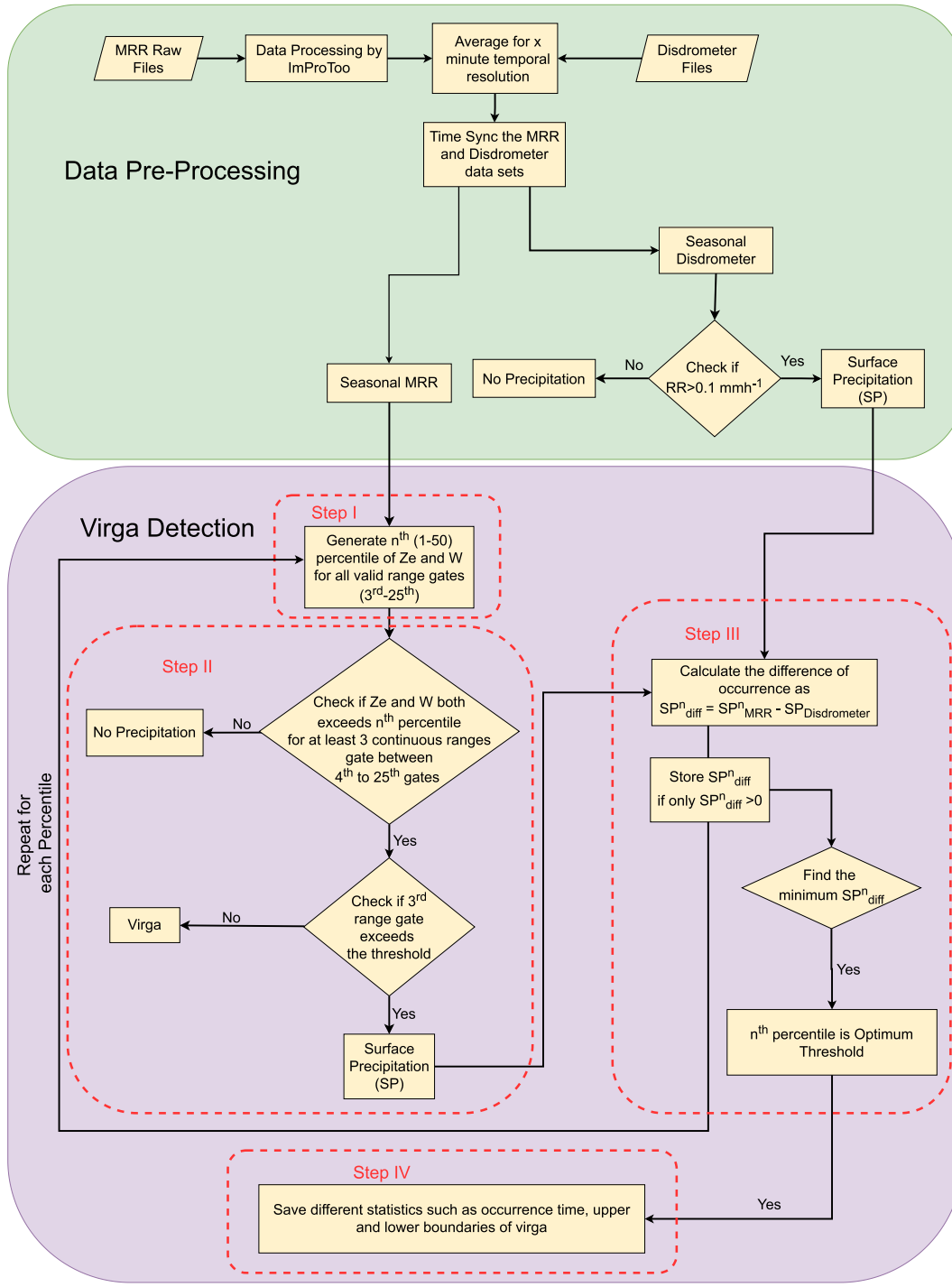

Figure 1. The flowchart of the virga detection algorithm using MRR and disdrometer data.

3.1. Data Pre-Processing

The first phase of the algorithm focuses on preparing the desired data set. The raw MRR Doppler spectra were processed using IMProToo, an advanced MRR processing tool by Maahn and Kollias (2012) to improve snow detection. This generates a NetCDF file with precipitation parameters such as reflectivity factor (Ze) and Doppler velocity (W) at a temporal resolution of 1 min. To minimize the effect of transient noise and the time delay for precipitation to reach the surface from above heights, these 1 min vertical profiles are further averaged at a

21698996, 2026, 6, Downloaded from https://agupubs.onlinelibrary.wiley.com/doi/10.1029/2025JD044204 by Indian Institute of Technology Indore, Wiley Online Library on [08/04/2026]. See the Terms and Conditions (https://onlinelibrary.wiley.com/terms-and-conditions) on Wiley Online Library for rules of use; OA articles are governed by the applicable Creative Commons License

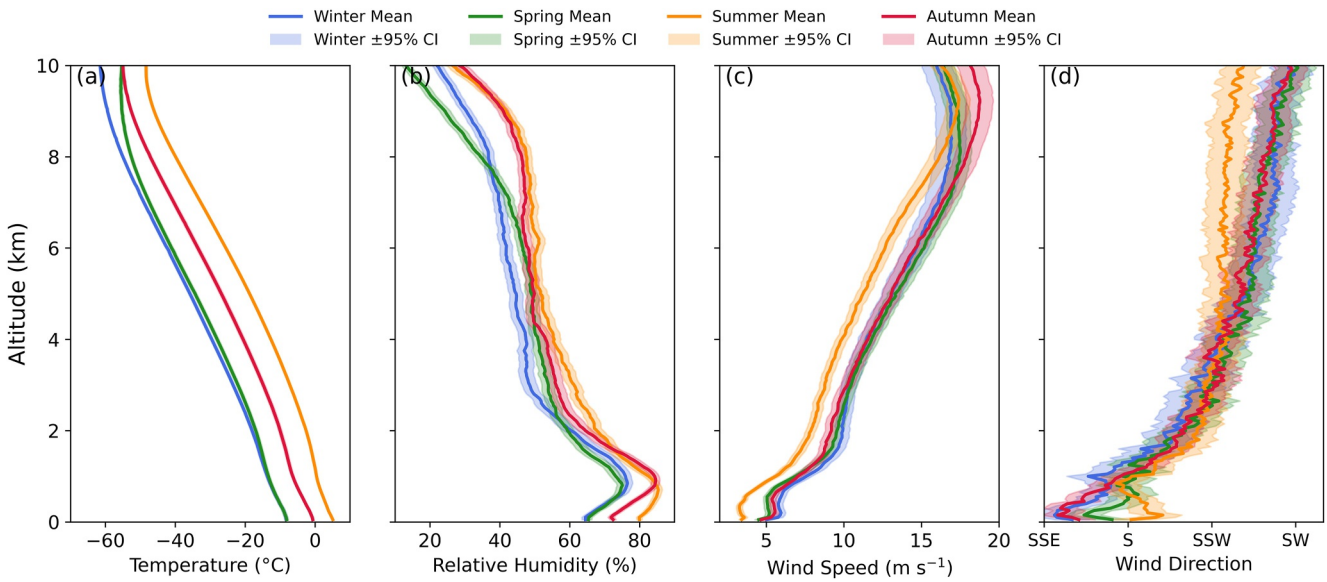

Figure 2. Seasonal variation of vertical profiles of (a) temperature (°C), (b) relative humidity (%), (c) wind speed (ms^{-1}) and (d) wind direction upto 10 km from radiosonde.

temporal resolution of x ($x = 6$ min for the current study). For an accurate comparison, only data when both MRR and disdrometer observations are available are considered, ensuring that identical time frames are analyzed across both instruments.

It should be noted here that for the time synchronization of the MRR and the ceilometer with the disdrometer, the accurate fall time correction of the hydrometeors needs to be considered. Here, the 6 min average somewhat minimizes the time delay issue but cannot fully resolve the problem. Averaging for a longer time will reduce this problem, but then many fine-scale variations will be lost. However, due to the unavailability of particle density and size distribution, the exact fall time correction is difficult to implement based on standalone MRR. This remains a limitation of the current algorithm and will be addressed in future studies. Consequently, virga statistics, as well as the temporal distribution between virga and precipitation, also include this effect, particularly in virga preceding precipitation conditions. The MRR provides vertical profile data across 32 height range gates, from the lowest at 0 m (range gate 0) to the highest at 6,200 m (range gate 31). For quality control and to reduce near-field interference and excessive noise, only range gates 3–25 were used, avoiding false detections of virga. This results in 23 usable range gates, covering a height range of 600–5,000 m with a range resolution of 200 m.

3.2. Virga Detection

The virga Detection process includes the following four steps to find the optimum threshold and detect virga.

3.2.1. Step I

The n^{th} ($n = 1, 2, \ldots, 50$) percentiles of Ze and W are generated separately for each height and different seasons. This height and seasonal differentiation are necessary because precipitation processes may vary according to seasonal tropospheric conditions (as shown in Figure 2), which can lead to different types of precipitation.

3.2.2. Step II

To differentiate between precipitation signatures and non-precipitating clouds, the threshold value is selected based on different percentile values generated above. To minimize precipitation detection error due to random fluctuation in Ze pr W profiles, instead of a particular range gate, the threshold value must be crossed (both Ze and W simultaneously) for at least 3 consecutive range gates (between 4$^{\text{th}}$-25$^{\text{th}}$ gates). Only those profiles that satisfy these conditions are classified as precipitating profiles, otherwise no-precipitation profiles. However, not all precipitation can reach the ground. Hence, among these profiles that exceed the threshold at the 3$^{\text{rd}}$ range gate,

21698996, 2026, 6, Downloaded from https://agupubs.onlinelibrary.wiley.com/doi/10.1029/2025JD044204 by Indian Institute of Technology Indore, Wiley Online Library on [08/04/2026]. See the Terms and Conditions (https://onlinelibrary.wiley.com/terms-and-conditions) on Wiley Online Library for rules of use; OA articles are governed by the applicable Creative Commons License

21698996, 2026, 6, Downloaded from https://agupubs.onlinelibrary.wiley.com/doi/10.1029/2025JD044204 by Indian Institute of Technology Indore, Wiley Online Library on [08/04/2026]. See the Terms and Conditions (https://onlinelibrary.wiley.com/terms-and-conditions) on Wiley Online Library for rules of use; OA articles are governed by the applicable Creative Commons License

they are also further classified as surface precipitation. The remaining precipitation profiles are classified as virga profiles that do not exceed the threshold at the 3rd range gate. Using both Ze and W thresholds is essential, as it ensures that particles with sufficient reflectivity but insufficient downward motion are correctly classified as virga rather than surface precipitation. Over the observation site, orographic and oceanic winds lead to frequent turbulent conditions that can reduce or even momentarily reverse the apparent fall speed of snow particles. However, in the context of virga, if strong updrafts prevent particles from descending, they remain above in the atmosphere and therefore remain consistent with the logic of our detection algorithm.

3.2.3. Step III

To determine the optimum or best threshold, the MRR statistics of surface precipitation for each percentile (1-50th) are compared with the disdrometer values. It is to be noted here that the no-surface precipitation in the disdrometer can't differentiate between virga and non-precipitating clouds. Accordingly, the MRR no-surface precipitation statistics here are essentially the sum of both no-precipitation and virga profiles. For each season, the optimal threshold is determined based on the difference in surface precipitation occurrences determined by the disdrometer and the MRR. The precipitation detection by MRR can be higher than the detection by the disdrometer due to the higher sensitivity of MRR, as well as the undetected virga below 600 m. Hence, the condition is defined in the following equation

$$\min\{\mathrm{SP}^{n}_{\mathrm{MRR}} - \mathrm{SP}_{\mathrm{Disdrometer}} \mid \mathrm{SP}^{n}_{\mathrm{MRR}} - \mathrm{SP}_{\mathrm{Disdrometer}} > 0\}$$

Where $\mathrm{SP}^{n}_{\mathrm{MRR}}$ represents the surface precipitation of MRR generated with the n^{th} $(n = 1, 2, \ldots, 50)$ percentile and $\mathrm{SP}_{\mathrm{Disdrometer}}$ represents the surface precipitation. The percentile n^{th} is considered the optimum threshold, which corresponds to the closest higher occurrence of surface precipitation from MRR compared to the disdrometer.

3.2.4. Step IV

The optimal threshold obtained in Step III is applied to the full data set using the procedure described in Step II to derive the final virga characteristics, including occurrence time and the lower and upper boundaries of virga events. This step does not require the calculation of thresholds but the implementation of the threshold to derive the final results.

3.3. Analysis

The algorithm was applied to four years of data from Ny-Ålesund, Svalbard (2020–2024). The statistics corresponding to the optimum threshold are considered for the final analysis. The algorithm generates the output, such as the occurrence time, lower and upper edges of virga. The upper edge corresponds to the highest altitude at which a precipitation signal is detected, while the lower edge represents the height at the lowest detectable precipitation signal before evaporation or sublimation. Importantly, the lower edge of the virga can occur within the cloud or below the ceilometer-derived cloud base. Therefore, a combined analysis of the virga lower edge and CBH provides valuable insight into the cloud–precipitation relationship. However, this was not examined here for single and multi-layered cloud separately as ceilometer detection of multi-layer cloud is limited as already mentioned in Section 2.3. Hence, the upper and lower edges of the virga analysis were based on all data without classification of multi or single layer cloud. However, single and multi-layer cloud occurrences for virga and surface precipitation have been carried out to get an idea which types of cloud are more frequent in virga.

The occurrence time is used to calculate the temporal differences between the closest virga occurrences and surface precipitation to understand the relationship between them. In addition, AWS measurements are used to understand associated meteorological conditions during virga and surface precipitation.

The results section is organized as follows: first, the vertical atmospheric conditions are presented, followed by the rationale for using a season-dependent threshold. To demonstrate the workings of the algorithm, next discussed a case study from summer 2021. For a better understanding of the vertical structure of surface precipitation and virga events, all detected events were examined using seasonal Contour Frequency by Altitude Diagrams of Ze. Contour Frequency by Altitude Diagrams enable the relative occurrence comparison across altitudes by dividing the occurrence count in each bin by the maximum count at that height. Finally, the virga statistics and associated meteorological conditions were explained.

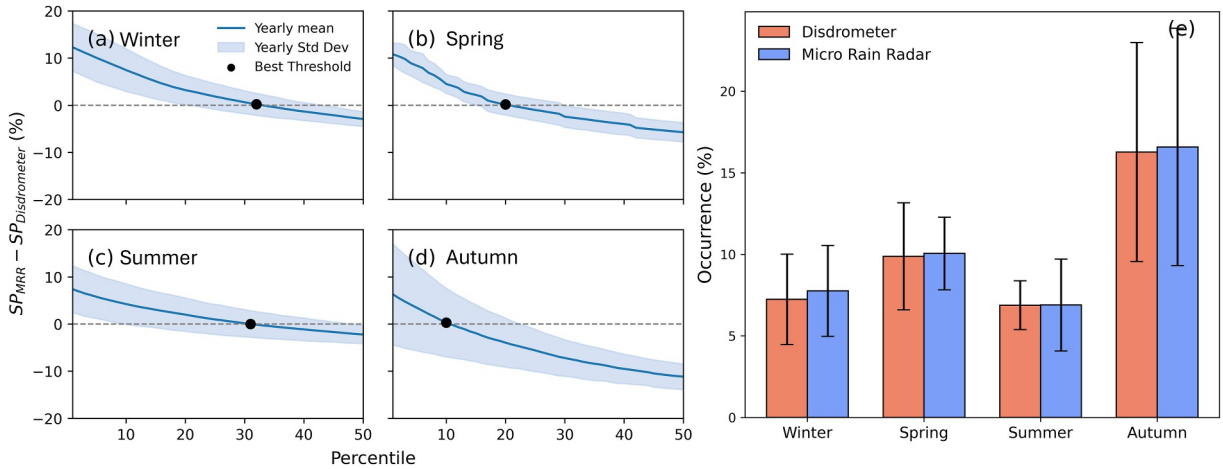

Figure 3. Seasonal mean and standard deviation of difference (%) between MRR and disdrometer-derived surface precipitation statistics for each season: (a) Winter, (b) Spring, (c) Summer, and (d) Autumn. The black dot denoting the best threshold corresponds to the closest higher surface precipitation occurrence from MRR relative to the disdrometer. (e) The occurrence of surface precipitation driven from the disdrometer and MRR by the best threshold.

4. Results

4.1. Tropospheric Condition Over the Study Location

To understand the nominal vertical atmospheric conditions of the site, radiosonde observations are studied. Figures 2a–2d presents the seasonal mean along with the 95% confidential interval of the vertical profiles of temperature, relative humidity, wind speed, and wind direction profiles, respectively, upto 10 km. Winter and spring show comparatively colder and drier tropospheric profiles than other seasons. However, the presence of relatively high humidity at lower levels in all seasons indicates low-level cloud formation. Summer exhibits the warmest and most humid atmospheric profiles, followed by autumn, especially near 1 km altitude.

The wind speed in Figure 2c shows a decreasing pattern toward the ground with the lowest wind speed in summer. Wind speeds in summer remain comparatively lower than those observed during the colder months, consistent with Graßl et al. (2022). The direction of wind in Figure 2d at higher levels shows that the winds are mainly approaching Ny-Ålesund from the southwest, while near the surface they are from the south to the southeast directions. Graßl et al. (2022) showed that higher-level winds follow the large-scale synoptic flow, while near the surface the winds turn south to southeast due to strong fjord-channeling and katabatic drainage in the Kongsfjorden valley during the cold seasons. Interestingly, summer experiences the most distinct deviation from the other seasons and shows south-southwesterly winds near the surface. This behavior likely reflects weak katabatic drainage due to surface warming and is more influenced by large scale circulation during summer. This seasonal variability in meteorological conditions influences the height-dependent evolution of precipitation, affecting its formation, growth, and evaporation or sublimation. Consequently, a season-dependent threshold for precipitation detection is incorporated into the proposed algorithm.

4.2. Optimal Seasonal Thresholds

The methodology described in the study is applied to the data collected from Ny-Ålesund. The generated optimum threshold varies between seasons, corresponding to the minimum positive difference for the occurrence of surface precipitation between the MRR and the disdrometer. For winter, spring, summer, and autumn, the optimum thresholds were found to be related to the percentiles 32, 20, 31, and 10 of Ze and W, respectively, as shown in Figures 3a–3d. Figure 3e presents a comparison of the seasonal mean occurrence of surface precipitation derived from the disdrometer and the MRR using the optimum threshold, along with their corresponding yearly standard deviations. Among all seasons, autumn shows the highest surface precipitation occurrence, followed by spring, winter, and summer.

Figure 4 presents seasonal variations in the optimum thresholds for Ze and W, ranging between ∼−6 to 3 dBZ and 0.2–1.2 ms^{-1}, respectively, depending on altitude and season. Autumn shows a relatively lower Ze threshold,

21698996, 2026, 6, Downloaded from https://agupubs.onlinelibrary.wiley.com/doi/10.1029/2025JD044204 by Indian Institute of Technology Indore, Wiley Online Library on [08/04/2026]. See the Terms and Conditions (https://onlinelibrary.wiley.com/terms-and-conditions) on Wiley Online Library for rules of use; OA articles are governed by the applicable Creative Commons License

21698996, 2026, 6, Downloaded from https://agupubs.onlinelibrary.wiley.com/doi/10.1029/2025JD044204 by Indian Institute of Technology Indore, Wiley Online Library on [08/04/2026]. See the Terms and Conditions (https://onlinelibrary.wiley.com/terms-and-conditions) on Wiley Online Library for rules of use; OA articles are governed by the applicable Creative Commons License

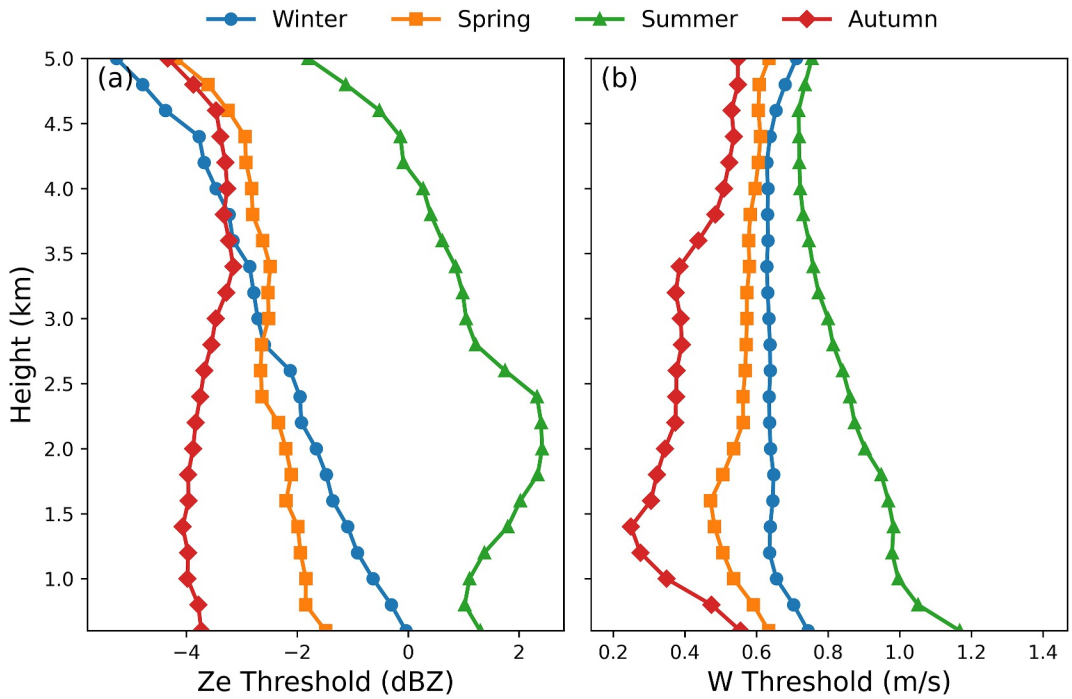

Figure 4. Seasonal variation of optimum thresholds profiles for (a) reflectivity (Ze) and (b) Doppler velocity (W).

while summer exhibits a higher threshold. Throughout all seasons, the W threshold gradually increases toward the surface, eventually ranging between 0.5 and 1.2 ms^{-1} on the ground. The relatively higher summer Ze and W thresholds likely reflect presence of mixed phase particles, particularly in the melting layer (1.5–2.5 km) as well as larger hydrometeor sizes compared to other seasons leading to increased Ze and W (Saini et al., 2025b).

4.3. Case Study of a Summer Virga

Figure 5 presents one of the many virga and precipitation events that occurred on 8 August 2021, between 00:24 and 06:00 UTC. In this case, in the initial half until ~03:30 UTC virga occurs, which changes to surface precipitation, and experiences virga again toward the end. This case shows both virga before the surface precipitation and after the surface precipitation. During the virga, the radar signals did not reach the ground, highlighted with the optimum threshold (31st percentile of Ze and W). Meanwhile, during the surface precipitation event, these signals clearly reach ground level (600 m). Figures 5a and 5b also shows the CBH, which indicates a higher base during virga and a lower base during surface precipitation. However, it should be noted that due to the strong backscatter of hydrometeors during precipitation, it can be misinterpreted as the cloud base on the ceilometer (Tuononen et al., 2019), particularly during heavy rain. Asutosh et al. (2021) also observed during high-intensity precipitation, the ceilometer experiences high backscatter and biases the cloud base measurements, while under light rain or snow, the ceilometer provides reliable cloud base estimates.

Figures 5c–5f shows the Ze and W profiles for the two time instants highlighted in Figures 5a and 5b by the green (virga) and blue (surface precipitation) areas, plotted along with the optimal summer threshold (31^{th} percentile). Both Ze and W profiles are clearly higher than the respective threshold for at least 3 continuous range gates, but do not reach the ground (600 m) during virga. In contrast, for surface precipitation, the Ze and W profiles are clearly higher than the respective threshold for at least 3 continuous range gates, as well as reaching the ground with a significantly higher signal than the respective threshold.

4.4. Vertical Profile of Reflectivity During Virga and Surface Precipitation

Figure 6 presents the seasonal CFADs of radar reflectivity for virga (top row) and surface precipitation (bottom row), revealing pronounced differences in the vertical structure and intensity of hydrometeor distributions between seasons. Virga typically shows an increasing Ze with a broad peak ~2–3 km. A systematic reduction below

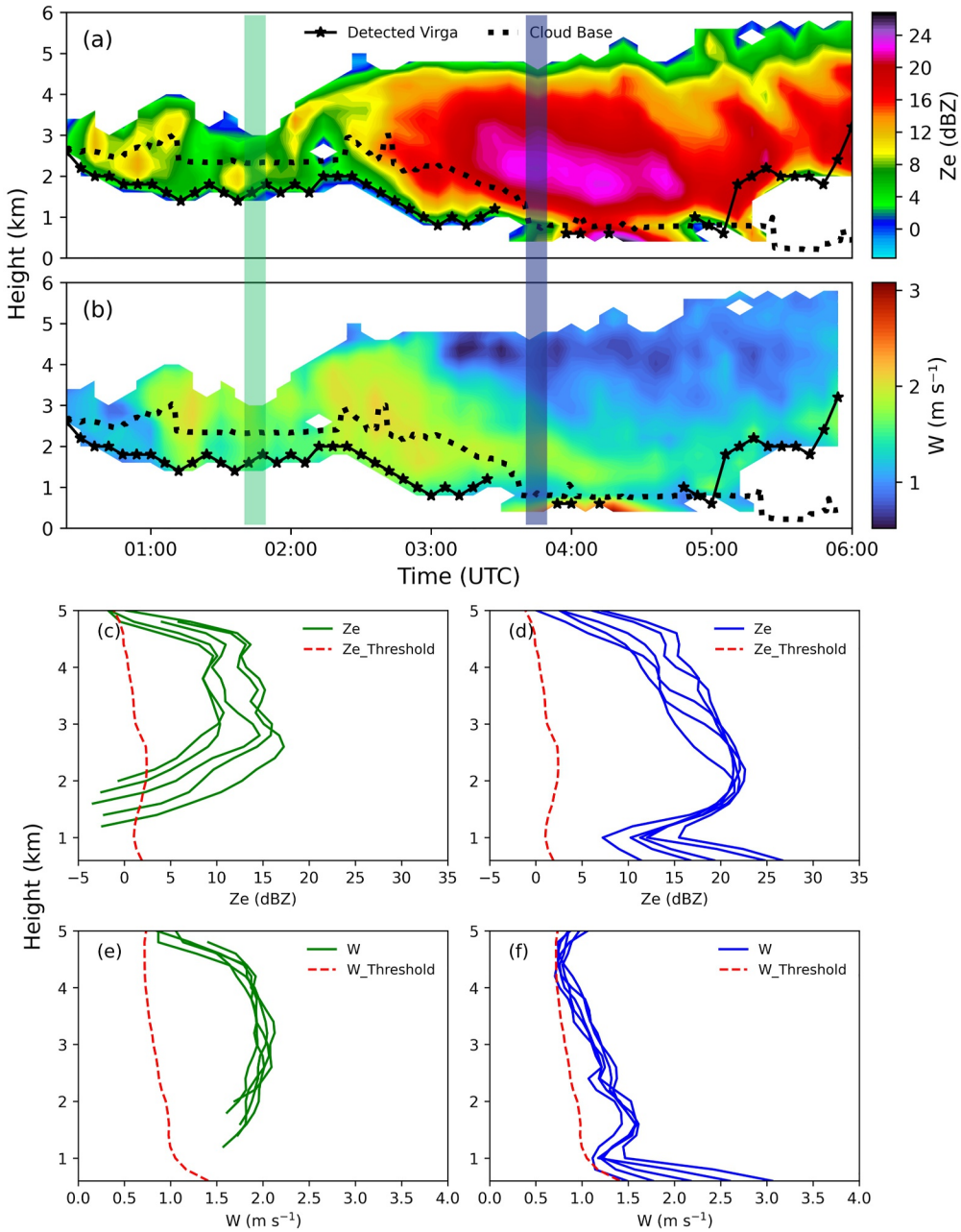

Figure 5. Vertical profiles of MRR-derived (a) Ze and (b) W including cloud base height on 27 August 2021 and detected virga heights with their 31st percentile thresholds (black line with asterisk). Vertical profiles of (c)–(d) Ze and (e)–(f) W during (c), (e) virga cases (green) and (d), (f) surface precipitation cases (blue), compared against the optimum threshold (red dashed line; 31st percentile for summer) for the event of 27 August 2021.

this altitude was observed in Ze, which does not lead to precipitation on the ground. In contrast, surface precipitation is characterized by higher and progressively increasing Ze values toward the surface.

Figure 6 presents the seasonal CFADs of Ze for virga (top row) and surface precipitation (bottom row), revealing pronounced seasonal differences in vertical structure. For virga cases (Figures 6a–6d), Ze values generally remain below ∼10 dBZ and typically exhibit an increase with height toward the ground, with a broad peak Ze at ∼2–3 km altitude. Below this level, a systematic reduction in Ze is observed, indicating weak precipitation formation aloft and substantial sublimation that prevents hydrometeors from reaching the surface. Winter and spring show

21698996, 2026, 6, Downloaded from https://agupubs.onlinelibrary.wiley.com/doi/10.1029/2025JD044204 by Indian Institute of Technology Indore, Wiley Online Library on [08/04/2026]. See the Terms and Conditions (https://onlinelibrary.wiley.com/terms-and-conditions) on Wiley Online Library for rules of use; OA articles are governed by the applicable Creative Commons License

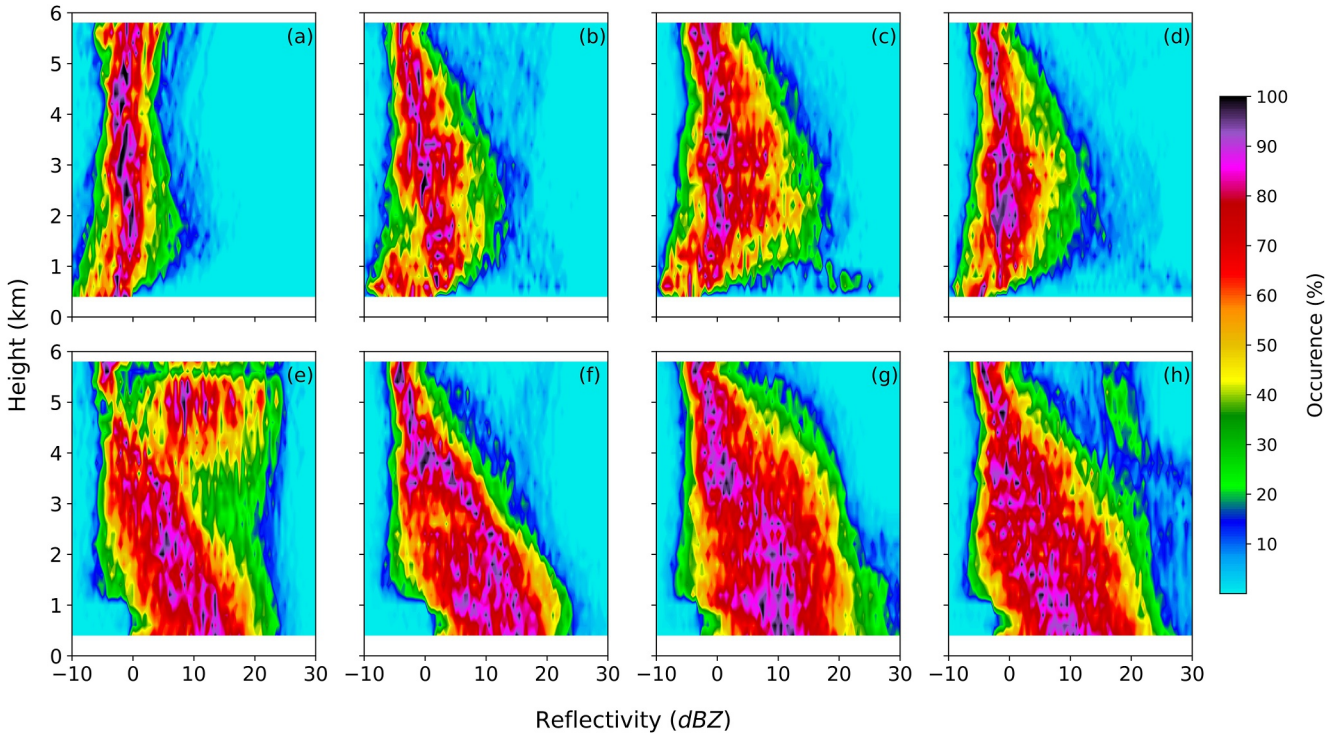

Figure 6. Vertical profiles of MRR reflectivity during (a–d) virga and (e–h) surface precipitation for winter, spring, summer, and autumn, respectively, up to 6 km.

comparatively lower reflectivity values, whereas summer and autumn show enhanced Ze, indicating large hydrometeors, most likely due to mixed phase and melting during the warmer seasons, leading to higher reflectivity peaks near 2–3 km altitude.

In contrast, the surface precipitation CFADs in Figures 6e–6h exhibit a continuously increasing Ze toward the surface up to ∼2 km, with higher Ze values (>25 dBZ) compared to those associated with virga. Below this altitude, winter and spring show nearly uniform reflectivity profiles, consistent with predominantly stratiform snowfall that occurs under stable boundary-layer conditions (Kneifel et al., 2011). Seasonally, summer and autumn show substantially higher Ze, reaching values of ∼30 dBZ near the surface, indicative of various microphysical growth driven by melting-layer processes and elevated liquid water content (Fabry, 2015; Klaassen, 1988). This pronounced vertical structure highlights a seasonal transition toward deeper and more intense precipitation systems during the warm months compared to the shallower and weaker precipitation profiles observed in winter and spring (Pruppacher et al., 1998). Interestingly, winter (Figure 6e) experiences a higher Ze in the mid-troposphere (∼4–5 km), unlike other seasons. This may suggest different ice-phase microphysical growth within cloud layers along with the higher cloud-base heights typically observed during winter (Morrison et al., 2012; Shates et al., 2025; Shupe et al., 2011).

4.5. Occurrence Statistics of Virga, Surface Precipitation and No-Precipitation

Figure 7 shows that the occurrence of surface precipitation events is higher in autumn, followed by spring, winter, and summer. The mean values of the occurrence of virga compared to the surface precipitation and no-precipitation cases vary between ∼2.6% and 9.5% as shown in Figure 7a. Figure 7b further compares the occurrence of virga and surface precipitation. This indicates how often precipitation, which started at higher levels, reaches the surface. Seasonally, the mean virga occurrence is highest in spring (39.96%), followed by autumn (36.04%), summer (29.66%) and winter with the lowest (25.05%). The colder and drier conditions during the spring and autumn seasons suggest a higher occurrence of the virga (Figure 2) than in the other seasons.

21698996, 2026, 6, Downloaded from https://agupubs.onlinelibrary.wiley.com/doi/10.1029/2025JD044204 by Indian Institute of Technology Indore, Wiley Online Library on [08/04/2026]. See the Terms and Conditions (https://onlinelibrary.wiley.com/terms-and-conditions) on Wiley Online Library for rules of use; OA articles are governed by the applicable Creative Commons License

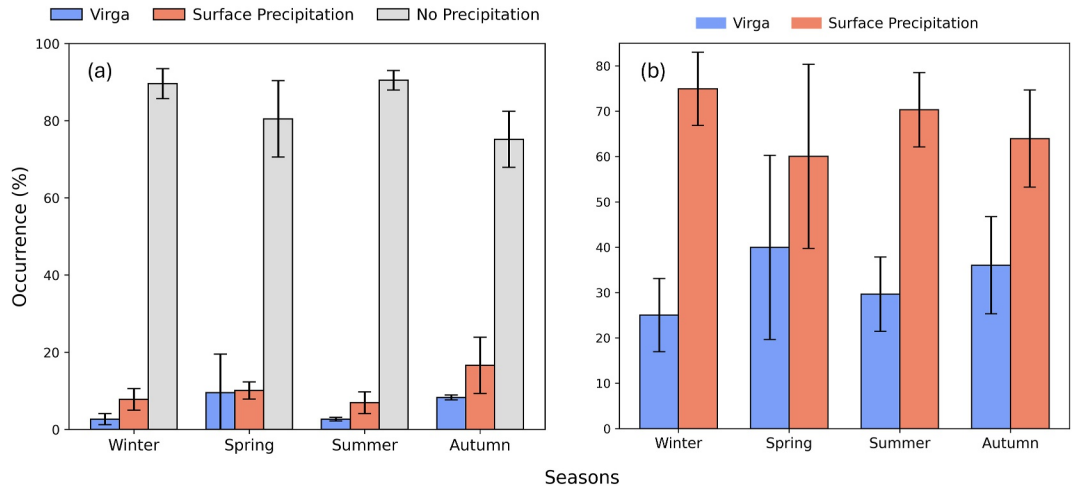

Figure 7. Seasonal occurrence of (a) surface precipitation, virga, and no precipitation, and (b) virga and surface precipitation.

4.6. Virga Upper and Lower Boundaries

The seasonal effect on the occurrence of virga is an interesting aspect to explore with the height of evaporation. Figure 8 presents the violin plot of the lower and upper edges of the virga profiles. The violin plot displays the probability density distribution of the occurrence over the heights, with the white mark indicating the median and the thick black bar showing the interquartile range (25%–75%). It can be observed that the upper edge of precipitation starts above 4 km more than half the time during summer and autumn, while in winter and spring it mostly starts below 4 km according to the median values. This indicates that precipitation most of the time starts at a higher altitude in warm seasons compared to cold.

However, the virga dissipation height or lower edge is found to exhibit pronounced seasonal variability. Summer experiences the highest dissipation height, with the primary peak of the lower edge occurring near 3 km, followed by autumn (∼1.5–2 km), winter (∼1–1.5 km), and spring (1 km). This ordering reflects the strong seasonal variation of the thermodynamic and dynamical conditions in the lower troposphere. The higher summer dissipation heights likely result from enhanced atmospheric temperatures during the polar day, whereas the lower winter and spring dissipation levels are indicative of stronger sublimation within the colder and drier layers. In addition, winter, summer, and autumn exhibit secondary peaks, located near 3 km for winter and autumn, and near

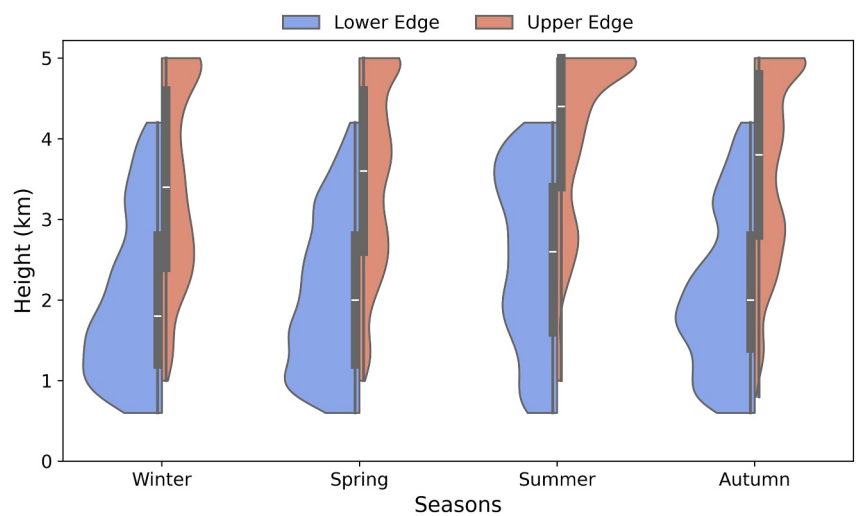

Figure 8. Seasonal variation in the probability density distributions of the lower (left side) and upper edge (right side) heights of virga, shown using violin plots. The white marker denotes the median, while the thick black bar indicates the interquartile range (25%–75%).

21698996, 2026, 6, Downloaded from https://agupubs.onlinelibrary.wiley.com/doi/10.1029/2025JD044204 by Indian Institute of Technology Indore, Wiley Online Library on [08/04/2026]. See the Terms and Conditions (https://onlinelibrary.wiley.com/terms-and-conditions) on Wiley Online Library for rules of use; OA articles are governed by the applicable Creative Commons License

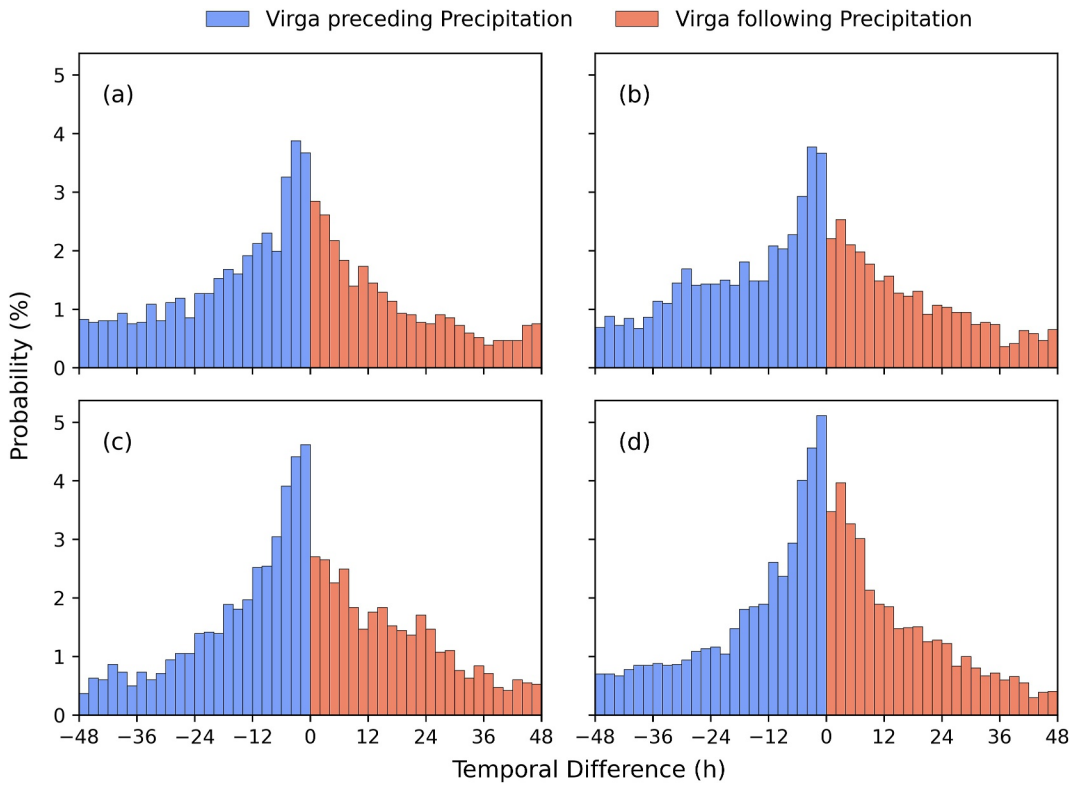

Figure 9. Histogram distribution of temporal difference between the closest virga for surface precipitation events across all seasons. Negative values indicate virga preceding precipitation, whereas positive values indicate virga following precipitation.

1.5 km for summer, indicating the presence of multiple preferred layers for the dissipation of virga under different seasonal atmospheric conditions, change in wind directions and moisture availability.

This also suggests that in the cold and transitional seasons, precipitation falls from various heights but evaporates a higher fraction at lower levels below ∼2 km. Meanwhile, summer shows a higher upper edge, indicating that precipitation begins at higher altitudes (>4 km) and evaporates a higher fraction above ∼2 km. It should be noted that the vertical resolution of 200 m is capable of resolving the occurrence of summer virga at higher altitudes. However, finer resolution vertical profiles that extend to lower levels are crucial to identifying low-level virga, particularly in the context of low-level polar clouds (Gierens et al., 2020; Griesche et al., 2020).

4.7. Temporal Difference Between Surface Precipitation and Virga Events

The focus here is on the temporal difference between surface precipitation and virga events. This reflects the time interval between when precipitation is observed at the surface and when a virga event occurs either before or after the precipitation. It is derived from the start time instant of both virga and surface precipitation events. Specifically, the temporal difference is defined as the time gap between a surface precipitation event and its nearest virga event.

Figure 9 presents the histogram distribution of the temporal differences between the virga and the surface precipitation. For comparison with previous study by Jullien et al. (2020), only the time window of ±48 hr is considered here, eliminating ∼28%–37% outlier cases. The corresponding mean and median values along with the percentage of preceding and following virga fractions are shown in Table 1.

Negative temporal differences correspond to the virga preceding the precipitation, whereas positive values indicate the virga following the precipitation. All seasons show a higher incidence of negative temporal differences, suggesting dominance of virga preceding precipitation. Each season exhibits a Gaussian distribution of the

21698996, 2026, 6, Downloaded from https://agupubs.onlinelibrary.wiley.com/doi/10.1029/2025JD044204 by Indian Institute of Technology Indore, Wiley Online Library on [08/04/2026]. See the Terms and Conditions (https://onlinelibrary.wiley.com/terms-and-conditions) on Wiley Online Library for rules of use; OA articles are governed by the applicable Creative Commons License

21698996, 2026, 6, Downloaded from https://agupubs.onlinelibrary.wiley.com/doi/10.1029/2025JD044204 by Indian Institute of Technology Indore, Wiley Online Library on [08/04/2026]. See the Terms and Conditions (https://onlinelibrary.wiley.com/terms-and-conditions) on Wiley Online Library for rules of use; OA articles are governed by the applicable Creative Commons License

Table 1
Seasonal Statistics of Temporal Differences Within −48 to +48 hr, With Outliers Removed, Showing Data Usage, Mean, Median and the Relative Frequency of Preceding and Following Events

Season	Data used in ±48hr (%)	Mean (h)	Median (h)	Preceding (%)	Following (%)
Winter	63.87	−2.99	−2.8	58.22	41.78
Spring	66.48	−3.24	−3.0	58.29	41.71
Summer	71.92	−0.57	−1.8	55.22	44.78
Autumn	75.88	−1.50	−1.6	54.21	45.79

temporal differences, with mean and median values being almost similar. The overall negative mean and median values indicate a higher occurrence of virga preceding precipitation events in each season (∼54%–59%).

The highest occurrence of temporal differences near zero suggests that virga and surface precipitation are frequently different stages of the same synoptic event. Similar patterns of temporal distribution were also described in Jullien et al. (2020). Their study indicates that the virga preceding precipitation often corresponds to the early phase of the precipitation event, which is most common in the cold seasons. However, virga following precipitation is more closely associated with the weakening phase of such occurrences observed in warm seasons.

4.8. Cloud Base Height and Meteorological Conditions

The seasonal variation in the lower and upper boundaries of the virga also raises curiosity about how CBH differs during virga compared to surface precipitation. Based on the classification of individual cloud layers (CBH1 and CBH2), Figures 10a and 10b presents the seasonal occurrence of single and double layer clouds associated with both virga and surface precipitation. It can be seen in Figures 10a and 10b that single-layer clouds dominate in all seasons for both types of precipitation. It should be noted that ceilometer may underestimate multi-layer clouds, as signal attenuation by low level cloud bases and, as already discussed, precipitation can reduce the detection of upper layers. This may bias the statistics toward single-layer clouds.

For virga, the highest occurrence of double layered clouds is observed in autumn (21.73 ± 8.46%) followed by summer (18.88 ± 4.06%), spring (14.31 ± 8.04%) and winter (7.58 ± 4.84%). Surface precipitation exhibits a similar kind of seasonal pattern, with the highest fraction of double layered clouds also in autumn (17.09 ± 5.18%), followed by summer (15.82 ± 2.44%), spring (10.08 ± 3.13%), and winter (9.02 ± 4.62%). In a similar study in the Arctic, Nomokonova et al. (2019) observed 44.8% multilayer and 36% single layer clouds in a total cloud occurrence of ∼81% in 14 months of observations using a ceilometer, microwave radiometer and 94 GHz cloud radar. Another study by Vassel et al. (2019) proposed a multilayer cloud detection algorithm applied to radiosonde and radar data and reported that multilayer clouds occur on nearly 29% of days during a time period of 1 year over Ny-Ålesund.

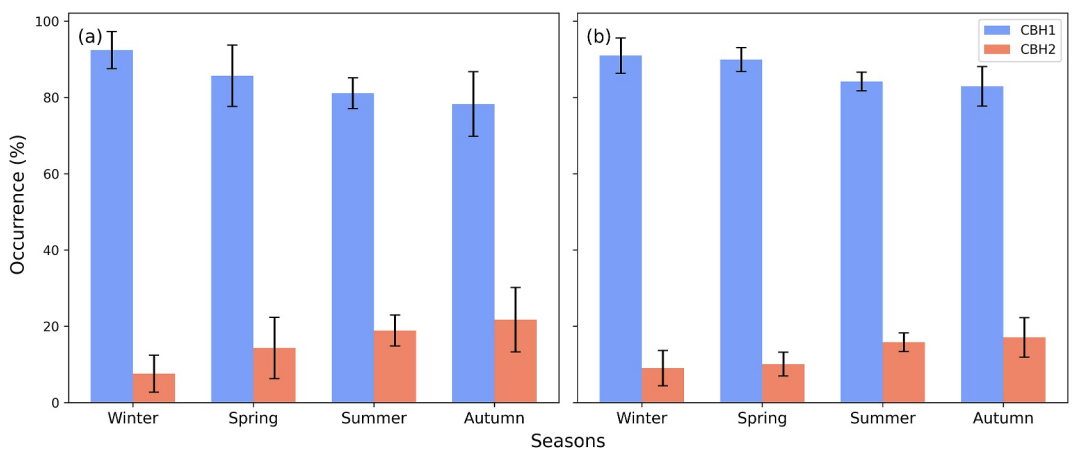

Figure 10. Seasonal occurrence of CBH1 and CBH2 for (a) virga and (b) surface precipitation, representing single-layer and double-layer cloud fractions, respectively.

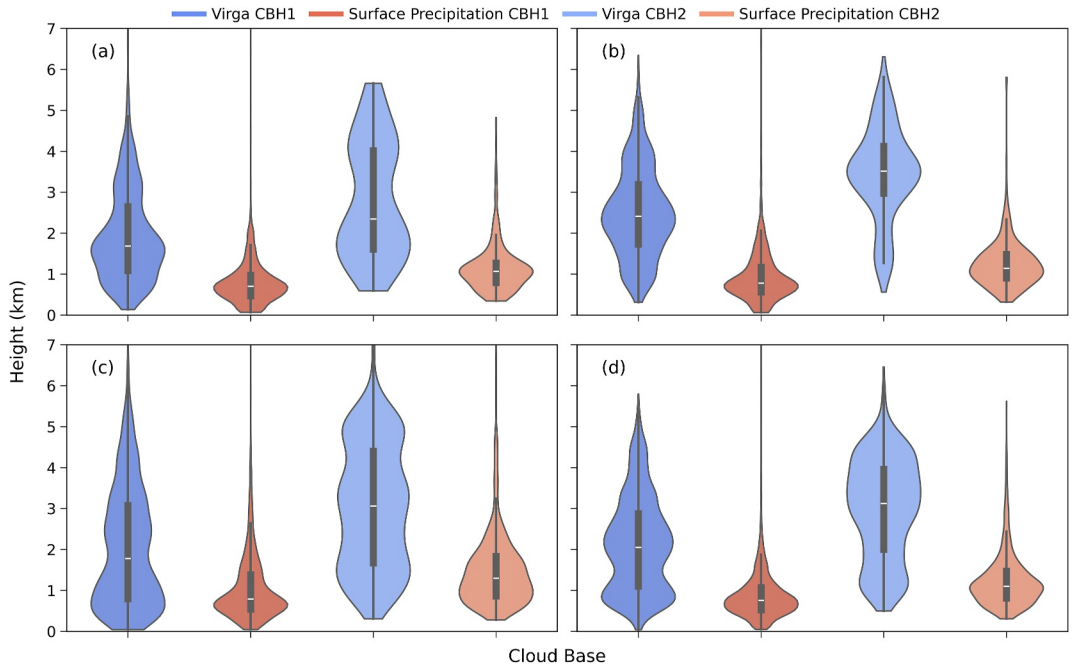

Figure 11. Seasonal variation of cloud base height associated with virga and surface precipitation for CBH1 and CBH2 in (a) Winter, (b) Spring, (c) Summer, and (d) Autumn.

Figure 11 presents the distribution of CBH1 and CBH2 for both virga and surface precipitation throughout all seasons. During virga, CBH1 has a high probability of occurrence around 1.5 km in winter, while in spring and summer it changes to 2.5 and 0.6 km, respectively. Autumn displays two distinct peaks, one just below 1 km and another just above 2 km. For CBH2, a higher probability is observed above 2 km, with a peak at 1.5 km in winter, while spring shows a more pronounced peak at 3.5 km. In contrast, summer demonstrates a uniform probability distribution of CBH2 at all heights, similar to autumn, but with a slightly higher probability above 2 km.

Compared to Virga, surface precipitation related cloud bases are generally lower, as the peak occurrence of CBH1 is around 0.5 km and CBH2 around at 1 km in all seasons. This suggests that virga clouds are typically located at higher heights than surface precipitation clouds. Additionally, in summer, virga-related clouds exhibit a low level CBH1 while CBH2 is distributed uniformly across all heights, highlighting a distinct seasonal behavior. During surface precipitation, variation in CBH is consistent with (Asutosh et al., 2021), showing that most low-level clouds occur below 1 km over Ny-Ålesund, with multilayer structures extending up to 3 km, but this pattern is not observed during virga. The variation in the lower edge of the virga in Figure 8 further indicates that in spring the dissipation of the virga occurs mainly below the cloud base, while in other seasons it is observed more frequently within the cloud layer, highlighting seasonal differences in cloud–precipitation interactions.

Figure 12 presents a seasonal variation of different 10 m ground conditions such as (a) temperature (°C) (b) relative humidity (%), (c) wind speed (ms^{-1}) and (d) wind direction (°). Surface precipitation typically occurs at slightly warmer temperatures, while virga spans a wider temperature range, particularly during winter and spring. In summer and, to some extent, autumn, both types of precipitation are mostly observed at higher positive temperatures. However, virga are more frequent at higher temperatures in autumn compared to surface precipitation, which exhibits a broader temperature distribution. Although the temperature differences between virga and surface precipitation are not very significant, relative humidity shows a clear distinction, as expected. Relative humidity is consistently low for virga, indicating dry conditions. Summer and autumn show comparably high humidity compared to winter and spring during both virga and surface precipitation events. Wind speed does not show any significant difference between virga and surface precipitation, although summer generally experiences lower wind speeds compared to other seasons. Both are mainly associated with southeast winds, with additional contributions from south and southwestern flows.

21698996, 2026, 6, Downloaded from https://agupubs.onlinelibrary.wiley.com/doi/10.1029/2025JD044204 by Indian Institute of Technology Indore, Wiley Online Library on [08/04/2026]. See the Terms and Conditions (https://onlinelibrary.wiley.com/terms-and-conditions) on Wiley Online Library for rules of use; OA articles are governed by the applicable Creative Commons License

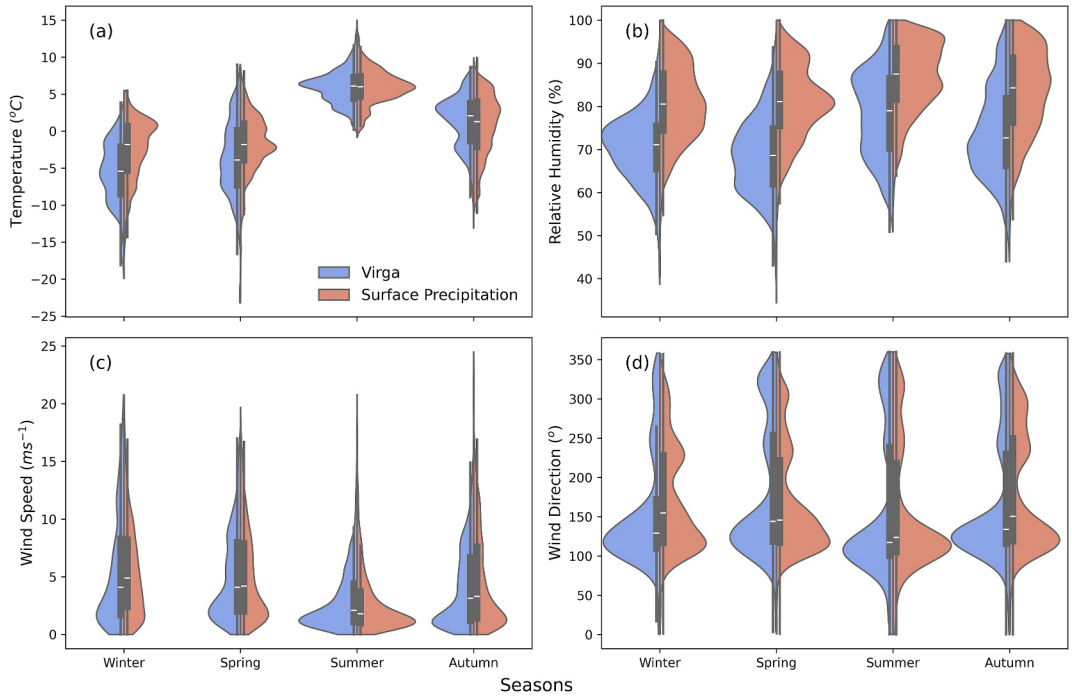

Figure 12. Seasonal variation between virga and surface precipitation for 10 m level meteorological conditions: (a) Temperature (°C), (b) Relative Humidity (%), (c) Wind Speed (ms^{-1}), and (d) Wind direction(°).

5. Summary and Discussion

This paper describes a new detection algorithm to identify precipitation and virga using the vertical profiles of Ze and W from the Micro Rain Radar (MRR). The tool is tested on observational data from the MRR and the disdrometer at Ny-Ålesund in the Arctic region. The algorithm detects the precipitation and non precipitation signal based on the height and seasonal dependent threshold of Ze and W. The Ze threshold was found to vary from −6 to 3 dBZ in heights and seasons, which is higher than the effective sensitivity of the ImProToo processed MRR (−14 dBZ) and the default threshold used in previous studies (−10 and −15 dBZ) (Jullien et al., 2020; Maahn & Kollias, 2012). The detection of virga is simultaneously limited by the W range (0.2–1.2 ms^{-1}).

Statistics from the Ny-Ålesund study suggest that autumn has the highest surface precipitation, whereas spring has the highest occurrence of virga annually. Approximately 25%–40% of precipitation that does not reach the surface leads to virga. These findings are consistent with long-term KAZR observations (2011–2021) on the North Slope of Alaska, where snow virga accounts for approximately 28% of all snowing profiles detected (Shates et al., 2025). Similarly, studies conducted in East Antarctica report comparable fractions of virga occurrence, with values of ∼35% in coastal regions, including 36% in Dumont d'Urville (DDU; coastal, 66.7°S, 140.0°E) and 47% in Princess Elisabeth (PE; inland, 71.9°S, 23.3°E) (Durán-Alarcón et al., 2019; Grazioli et al., 2017). In comparison, space borne radar observations suggest that virga occurrence exceeds ∼50% in arid and desert regions, but remains below ∼30% in polar regions (Figure 2d) in Wang et al. (2018)). The results of the current study are expected to improve this more precisely with seasonal variability in the Arctic.

In Ny-Ålesund, it is observed that during summer evaporation occurs primarily above 2 km, while in other seasons the probability of evaporation is higher below this level. Surface precipitation is mainly associated with low cloud bases (0.5–1 km), whereas virga is linked to higher cloud layers above 1 km, which may be due to higher attenuation of the ceilometer signal during precipitation (Asutosh et al., 2021). Seasonally, virga tends to occur within cloud layers during winter, autumn, and summer, while in spring it is more frequently observed below cloud base, likely due to shallower cloud systems. The frequent occurrence of multilayer cloud structures during virga events, particularly in autumn and summer, is consistent with earlier Arctic studies. For example, Nomokonova et al. (2019) reported that multilayer clouds account for 44.8% of cloud occurrences over Ny-Ålesund, while Vassel et al. (2019) found that multilayer clouds occur on nearly 29% of days. Both virga and

21698996, 2026, 6, Downloaded from https://agupubs.onlinelibrary.wiley.com/doi/10.1029/2025JD044204 by Indian Institute of Technology Indore, Wiley Online Library on [08/04/2026]. See the Terms and Conditions (https://onlinelibrary.wiley.com/terms-and-conditions) on Wiley Online Library for rules of use; OA articles are governed by the applicable Creative Commons License

surface precipitation generally occur below the freezing level of surface temperature throughout the year, except in summer. Additionally, during virga, the relative humidity was found to be lower compared to that during surface precipitation. Virga occurs mainly before the precipitation, and the low values of the mean (and median) of the temporal difference suggest that it could be part of the same synoptic event.

This study provides a more accurate quantification of virga using high resolution MRR vertical profiles. However, the 200 m vertical resolution used in this investigation is limited by the 600 m lowest usable range gate of the MRR, which makes it unable to resolve near-surface virga processes. However, disdrometer data was used to measure surface precipitation and to provide context for the processes that may occur below the lowest MRR range gate. Nevertheless, to better capture low-level virga processes, the technique can be used with higher-resolution MRR data, as the algorithm is resolution independent and when such data are available.

Conflict of Interest

The authors declare no conflicts of interest relevant to this study.

Data Availability Statement

Meteorological observations from the AWS and radiosonde from the AWIPEV Research Station are openly available through the PANGAEA data portal at Maturilli (2020); Maturilli and Dünschede (2023), respectively. Pre-processed in situ precipitation and cloud data sets from Himadri Research Station, together with the analysis scripts and visualization codes supporting this study, are archived at Zenodo (Saini et al., 2025a).

Acknowledgments
The authors acknowledge the support provided by the Director of ESSO - NCPOR for Research in Svalbard (RiS IDs 12263 and 12301) and facilitating the access to essential data during this study (J-89/2025-26). The first author (LS) thanks the CSIR, India for the fellowship funding (file number: 02/1022(12356)/2021-EMR-I). One of the authors (SD) acknowledges the financial support provided by SERB, India (CRG/2022/006986) and MoES, India (MoES/16/4/2021-RDESS/NARM-4). The authors acknowledges the AWIPEV research facility for providing the AWS and radiosonde data. The authors also thank anonymous reviewers and the editor for their valuable comments.

References

Agosta, C., Amory, C., Kittel, C., Orsi, A., Favier, V., Gallée, H., et al. (2019). Estimation of the antarctic surface mass balance using the regional climate model mar (1979–2015) and identification of dominant processes. *The Cryosphere*, *13*(1), 281–296. https://doi.org/10.5194/tc-13-281-2019

Asutosh, A., Chatterjee, S., Subeesh, M., Radhakrishnan, A., & Murukesh, N. (2021). Observation of cloud base height and precipitation characteristics at a polar site ny-Ålesund, Svalbard using ground-based remote sensing and model reanalysis. *Remote Sensing*, *13*(14), 2808. https://doi.org/10.3390/rs13142808

Battaglia, A., Rustemeier, E., Tokay, A., Blahak, U., & Simmer, C. (2010). Parsivel snow observations: A critical assessment. *Journal of Atmospheric and Oceanic Technology*, *27*(2), 333–344. https://doi.org/10.1175/2009jtecha1332.1

Beynon, R., & Hocke, K. (2022). Snow virga above the swiss plateau observed by a micro rain radar. *Remote Sensing*, *14*(4), 890. https://doi.org/10.3390/rs14040890

Cha, J., & Yum, S. (2020). Characteristics of precipitation particles measured by parsivel disdrometer at a mountain and a coastal site in Korea. *Asia-Pacific Journal of Atmospheric Sciences*, *57*(2), 261–276. https://doi.org/10.1007/s13143-020-00190-6

Durán-Alarcón, C., Boudevillain, B., Genthon, C., Grazioli, J., Souverijns, N., van Lipzig, N. P. M., et al. (2019). The vertical structure of precipitation at two stations in east Antarctica derived from micro rain radars. *The Cryosphere*, *13*(1), 247–264. https://doi.org/10.5194/tc-13-247-2019

Evans, E., Stewart, R., Henson, W., & Saunders, K. (2011). On precipitation and virga over three locations during the 1999–2004 canadian prairie drought. *Atmosphere-Ocean*, *49*(4), 366–379. https://doi.org/10.1080/07055900.2011.608343

Fabry, F. (2015). *Radar meteorology: Principles and practice*. Cambridge University Press. https://doi.org/10.1017/CBO9781107707405

Garcia-Benadi, A., Bech, J., Gonzalez, S., Udina, M., Codina, B., & Georgis, J.-F. (2020). Precipitation type classification of micro rain radar data using an improved doppler spectral processing methodology. *Remote Sensing*, *12*(24), 4113. https://doi.org/10.3390/rs12244113

Gierens, R., Kneifel, S., Shupe, M. D., Ebell, K., Maturilli, M., & Löhnert, U. (2020). Low-level mixed-phase clouds in a complex arctic environment. *Atmospheric Chemistry and Physics*, *20*(6), 3459–3481. https://doi.org/10.5194/acp-20-3459-2020

Grazioli, J., Madeleine, J.-B., Gallée, H., Forbes, R. M., Genthon, C., Krinner, G., & Berne, A. (2017). Katabatic winds diminish precipitation contribution to the antarctic ice mass balance. *Proceedings of the National Academy of Sciences*, *114*(41), 10858–10863. https://doi.org/10.1073/pnas.1707633114

Graßl, S., Ritter, C., & Schulz, A. (2022). The nature of the ny-Ålesund wind field analysed by high-resolution windlidar data. *Remote Sensing*, *14*(15), 3771. https://doi.org/10.3390/rs14153771

Griesche, H. J., Seifert, P., Ansmann, A., Baars, H., Barrientos Velasco, C., Bühl, J., et al. (2020). Application of the shipborne remote sensing supersite oceanet for profiling of arctic aerosols and clouds during *Polarstern* cruise ps106. *Atmospheric Measurement Techniques*, *13*(10), 5335–5358. https://doi.org/10.5194/amt-13-5335-2020

Illingworth, A. J., Hogan, R. J., O'Connor, E., Bouniol, D., Brooks, M. E., Delanoé, J., et al. (2007). Cloudnet: Continuous evaluation of cloud profiles in seven operational models using ground-based observations. *Bulletin of the American Meteorological Society*, *88*(6), 883–898. https://doi.org/10.1175/BAMS-88-6-883

Jullien, N., Vignon, E., Sprenger, M., Aemisegger, F., & Berne, A. (2020). Synoptic conditions and atmospheric moisture pathways associated with virga and precipitation over coastal adélie land in Antarctica. *The Cryosphere*, *14*(5), 1685–1702. https://doi.org/10.5194/tc-14-1685-2020

Kalesse-Los, H., Kötsche, A., Foth, A., Röttenbacher, J., Vogl, T., & Witthuhn, J. (2023). The virga-sniffer – A new tool to identify precipitation evaporation using ground-based remote-sensing observations. *Atmospheric Measurement Techniques*, *16*(6), 1683–1704. https://doi.org/10.5194/amt-16-1683-2023

Klaassen, W. (1988). Radar observations and simulation of the melting layer of precipitation. *Journal of the Atmospheric Sciences*, *45*(24), 3741–3753. https://doi.org/10.1175/1520-0469(1988)045<3741:roasot>2.0.co;2

21698996, 2026, 6, Downloaded from https://agupubs.onlinelibrary.wiley.com/doi/10.1029/2025JD044204 by Indian Institute of Technology Indore, Wiley Online Library on [08/04/2026]. See the Terms and Conditions (https://onlinelibrary.wiley.com/terms-and-conditions) on Wiley Online Library for rules of use; OA articles are governed by the applicable Creative Commons License

Kneifel, S., Maahn, M., Peters, G., & Simmer, C. (2011). Observation of snowfall with a low-power fm-cw k-band radar (micro rain radar). *Meteorology and Atmospheric Physics*, *113*(1–2), 75–87. https://doi.org/10.1007/s00703-011-0142-z

Kodamana, R., & Fletcher, C. G. (2021). Validation of cloudsat-cpr derived precipitation occurrence and phase estimates across Canada. *Atmosphere*, *12*(3), 295. https://doi.org/10.3390/atmos12030295

Löffler-Mang, M., & Joss, J. (2000). An optical disdrometer for measuring size and velocity of hydrometeors. *Journal of Atmospheric and Oceanic Technology*, *17*(2), 130–139. https://doi.org/10.1175/1520-0426(2000)017<0130:aodfms>2.0.co;2

Maahn, M., Burgard, C., Crewell, S., Gorodetskaya, I. V., Kneifel, S., Lhermitte, S., et al. (2014). How does the spaceborne radar blind zone affect derived surface snowfall statistics in polar regions? *Journal of Geophysical Research: Atmospheres*, *119*(24), 13–604. https://doi.org/10.1002/2014jd022079

Maahn, M., & Kollias, P. (2012). Improved micro rain radar snow measurements using doppler spectra post-processing. *Atmospheric Measurement Techniques*, *5*(11), 2661–2673. https://doi.org/10.5194/amt-5-2661-2012

Maturilli, M. (2020). Continuous meteorological observations at station Ny-Ålesund (2011-08 et seq) [dataset publication series]. *PANGAEA*. https://doi.org/10.1594/PANGAEA.914979

Maturilli, M., & Dünschede, E. (2023). Homogenized radiosonde record at station Ny-Ålesund, Spitsbergen, 2017-2022 [dataset publication series]. *PANGAEA*. https://doi.org/10.1594/PANGAEA.961203

Maturilli, M., & Ebell, K. (2018). Twenty-five years of cloud base height measurements by ceilometer in ny-ålesund, Svalbard. *Earth System Science Data*, *10*(3), 1451–1456. https://doi.org/10.5194/essd-10-1451-2018

Maturilli, M., Herber, A., & König-Langlo, G. (2013). Climatology and time series of surface meteorology in ny-ålesund, Svalbard. *Earth System Science Data*, *5*(1), 155–163. https://doi.org/10.5194/essd-5-155-2013

Maturilli, M., & Kayser, M. (2017). Arctic warming, moisture increase and circulation changes observed in the ny-ålesund homogenized radiosonde record. *Theoretical and Applied Climatology*, *130*(1–2), 1–17. https://doi.org/10.1007/s00704-016-1864-0

Morrison, H., De Boer, G., Feingold, G., Harrington, J., Shupe, M. D., & Sulia, K. (2012). Resilience of persistent arctic mixed-phase clouds. *Nature Geoscience*, *5*(1), 11–17. https://doi.org/10.1038/ngeo1332

Nomokonova, T., Ebell, K., Löhnert, U., Maturilli, M., Ritter, C., & O'Connor, E. (2019). Statistics on clouds and their relation to thermodynamic conditions at ny-ålesund using ground-based sensor synergy. *Atmospheric Chemistry and Physics*, *19*(6), 4105–4126. https://doi.org/10.5194/acp-19-4105-2019

Ott parsivel-2 disdrometer manual. (2023). Ott parsivel-2 disdrometer manual. Retrieved from https://psl.noaa.gov/data/obs/instruments/OpticalDisdrometer.pdf

Oyj, V. (2022). Ceilometer cl51 datasheet (b210861en-g.1). Retrieved from https://docs.vaisala.com/v/u/B210861EN-G.1/en-US (Retrieved June 6, 2024)

Peters, G., Fischer, B., & Andersson, T. (2002). Rain observations with a vertically looking micro rain radar (mrr). *Boreal Environment Research*, *7*(4), 353–362. http://hdl.handle.net/10138/578168

Pruppacher, H. R., Klett, J. D., & Wang, P. K. (1998). *Microphysics of clouds and precipitation*. Taylor and Francis. https://doi.org/10.1080/02786829808965531

Roberts, E., Stewart, R. E., & Lin, C. A. (2006). A study of drought characteristics over the canadian prairies. *Atmosphere-Ocean*, *44*(4), 331–345. https://doi.org/10.3137/ao.440402

Saikranthi, K., Narayana Rao, T., Radhakrishna, B., & Rao, S. V. B. (2014). Morphology of the vertical structure of precipitation over India and adjoining oceans based on long-term measurements of trmm pr. *Journal of Geophysical Research: Atmospheres*, *119*(13), 8433–8449. https://doi.org/10.1002/2014JD021774

Saini, L., Das, S., & Murukesh, N. (2024). Virga observation over ny-ålesund, arctic using micro rain radar. In *Igarss 2024-2024 ieee international geoscience and remote sensing symposium* (pp. 5563–5566). https://doi.org/10.1109/IGARSS55030.2025.11243520

Saini, L., Das, S., & Murukesh, N. (2025a). Arctic virga detection study data. *Zenodo*. https://doi.org/10.5281/zenodo.16909226

Saini, L., Das, S., & Murukesh, N. (2025b). Case studies of different types of precipitation at ny-ålesund, arctic. *Scientific Reports*, *15*(1), 3086. https://doi.org/10.1038/s41598-025-85833-2

Saini, L., Das, S., & Murukesh, N. (2025c). Vertical evolution of precipitation and associated atmospheric parameters at ny-å lesund (78° 55'n, 11° 56'e) in the arctic. *Atmospheric Research*, *329*, 108531. https://doi.org/10.1016/j.atmosres.2025.108531

Sarkar, T., Das, S., & Maitra, A. (2015). Assessment of different raindrop size measuring techniques: Inter-comparison of doppler radar, impact and optical disdrometer. *Atmospheric Research*, *160*, 15–27. https://doi.org/10.1016/j.atmosres.2015.03.001

Shates, J., Pettersen, C., L'Ecuyer, T., & Kulie, M. (2025). Kazr-cloudsat analysis of snowing profiles at the north slope of alaska: Implications of the satellite radar blind zone. *Journal of Geophysical Research: Atmospheres*, *130*(6), e2024JD042700. https://doi.org/10.1029/2024jd042700

Shupe, M. D., Walden, V. P., Eloranta, E., Uttal, T., Campbell, J. R., Starkweather, S. M., & Shiobara, M. (2011). Clouds at arctic atmospheric observatories. part i: Occurrence and macrophysical properties. *Journal of Applied Meteorology and Climatology*, *50*(3), 626–644. https://doi.org/10.1175/2010jamc2467.1

Stewart, R., Lawford, R. G., & Boisvert, A. (2011). The 1999-2005 canadian prairies drought: Science, impacts, and lessons. *Drought Research Initiative*. Retrieved from https://gwfnet.net/sites/dri/protected/Final%20draft%20for%20web%20-%20Oct.%2029.pdf

Tokay, A., Wolff, D. B., & Petersen, W. A. (2014). Evaluation of the new version of the laser-optical disdrometer, ott parsivel 2. *Journal of Atmospheric and Oceanic Technology*, *31*(6), 1276–1288. https://doi.org/10.1175/jtech-d-13-00174.1

Tuononen, M., O'Connor, E. J., & Sinclair, V. A. (2019). Evaluating solar radiation forecast uncertainty. *Atmospheric Chemistry and Physics*, *19*(3), 1985–2000. https://doi.org/10.5194/acp-19-1985-2019

Valdivia, J. M., Gatlin, P. N., Kumar, S., Scipión, D., Silva, Y., & Petersen, W. A. (2022). The gpm-dpr blind zone effect on satellite-based radar estimation of precipitation over the andes from a ground-based ka-band profiler perspective. *Journal of Applied Meteorology and Climatology*, *61*(4), 441–456. https://doi.org/10.1175/JAMC-D-20-0211.1

Vassel, M., Ickes, L., Maturilli, M., & Hoose, C. (2019). Classification of arctic multilayer clouds using radiosonde and radar data in Svalbard. *Atmospheric Chemistry and Physics*, *19*(7), 5111–5126. https://doi.org/10.5194/acp-19-5111-2019

Wang, Y., You, Y., & Kulie, M. (2018). Global virga precipitation distribution derived from three spaceborne radars and its contribution to the false radiometer precipitation detection. *Geophysical Research Letters*, *45*(9), 4446–4455. https://doi.org/10.1029/2018GL077891

Yang, F., Luke, E. P., Kollias, P., Kostinski, A. B., & Vogelmann, A. M. (2018). Scaling of drizzle virga depth with cloud thickness for marine stratocumulus clouds. *Geophysical Research Letters*, *45*(8), 3746–3753. https://doi.org/10.1029/2018gl077145

21698996, 2026, 6, Downloaded from https://agupubs.onlinelibrary.wiley.com/doi/10.1029/2025JD044204 by Indian Institute of Technology Indore, Wiley Online Library on [08/04/2026]. See the Terms and Conditions (https://onlinelibrary.wiley.com/terms-and-conditions) on Wiley Online Library for rules of use; OA articles are governed by the applicable Creative Commons License